

Calculation of Characteristics of Parametric X-Ray Radiation for Tests at the Advanced Superconducting Test Accelerator

Todd Seiss

Mentor: Tanaji Sen

Lee Teng Internship Program
Fermi National Accelerator Laboratory

August 24, 2014

Abstract

Parametric x-ray radiation (PXR) is a type of x-ray radiation produced when an electron beam is passed through a crystal. PXR is emitted at sharp angles with respect to the electron beam, and it generally has a quasi-monochromatic energy spectrum. Because of these unique and potentially useful properties, future experiments at ASTA will examine this radiation. To facilitate these experiments, I have written a simulation of many of the important characteristics. This paper will summarize the basic theory, how the simulation runs, what the results of the simulation are, and how the experiment could be conducted at ASTA.

1 Theory

1.1 Crystal Structure

The basic unit of crystal structure is the unit cell, which is the smallest repeating arrangement of atoms. The simplest unit cell, for example, is the simple cubic cell, in which the atoms lay at the eight vertices of a cube. This unit cell is shown in Figure 1 along with two other cubic unit cells, the face-centered cubic (FCC) and body-centered cubic (BCC). FCC unit cells have six more atoms, one at the center of each face of the cube, and BCC cells have only one more atom, at the center of the cube.

The unit cells are then packed so as to fill up space in three dimensions, as shown for the simple cubic cell in Figure 2. This arrangement of unit cells is known as the crystal lattice. Note that when the cells are arranged in the lattice, the atoms lay in parallel repeating planes. There are an infinite number of possible crystal planes. In order to understand and track the crystal planes, we introduce a coordinate system for the unit cells.

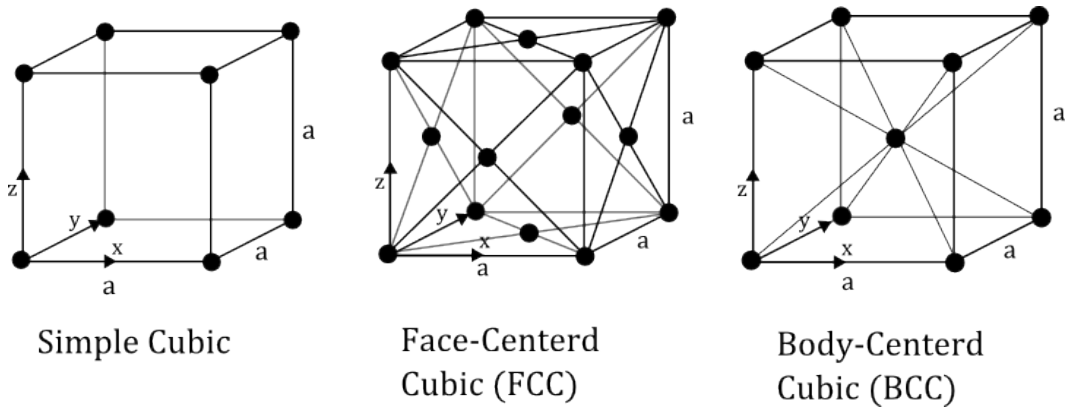


Figure 1: The basic three cubic unit cells.

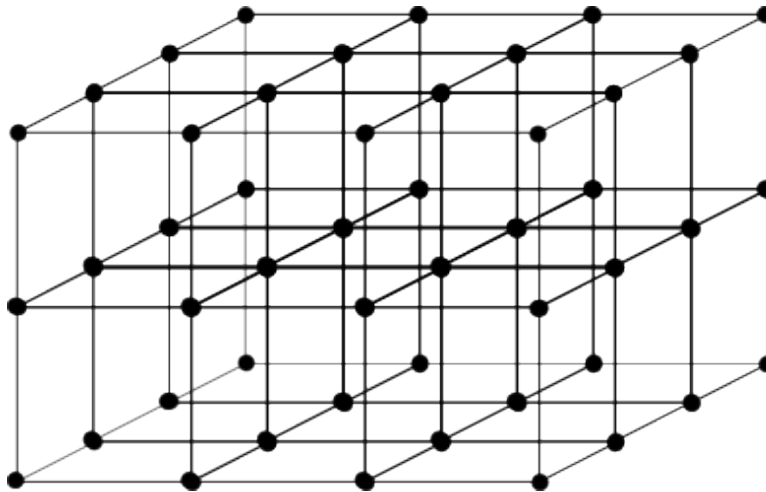


Figure 2: The simple cubic unit cell lattice, the most simple crystal structure. Note that it is easy to see that by filling space with the unit cell, the atoms are arranged into planes.

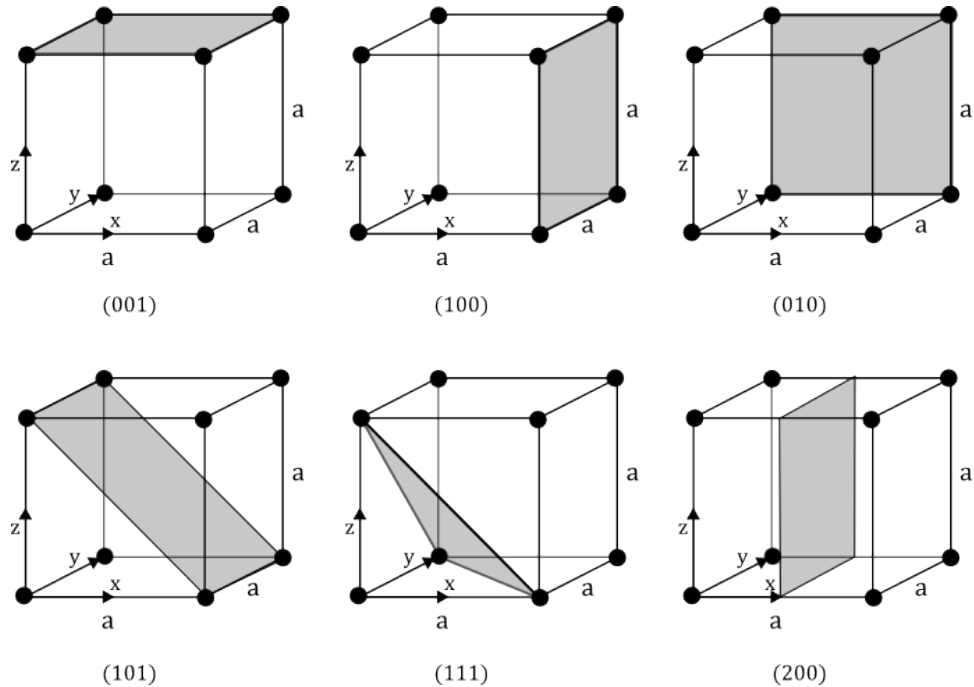


Figure 3: Several simple crystal planes.

The origin of the coordinate system is chosen to be one of the vertices of the cube. In Figure 1, the three coordinate axes are drawn at the origin, and the coordinate axes are picked to be along the primary axes of the unit cell. With this coordinate system, the position of any atom in the unit cell can be described. For example, in the FCC unit cell, the atom in the center of the nearest face has position $\frac{a}{2}\hat{x} + \frac{a}{2}\hat{z}$. It is, however, convenient to work in units scaled to the size of the unit cell, so we set $a = 1$. The position of this atom is then just $\frac{1}{2}\hat{x} + \frac{1}{2}\hat{z}$.

We now label crystal planes by the normal to the plane. The first plane in Figure 3 has a normal in the \hat{z} direction, so the plane is labeled by (001). The 1 indicates that the plane intersects the z -axis a distance a above the origin. Similarly the normal to the shaded plane in the fourth cube points in the $\hat{x} + \hat{z}$ direction, so this plane is labeled by (101)

When a plane intersects the axes at a distance less than the length of the unit cell, as in the last cube in Figure 3, the reciprocal of the distance along the axes is used. In this unit cell, the normal to the plane is in the \hat{x} direction, but the plane intersects the point $x = \frac{1}{2}$. Therefore, the plane is labeled by (200), not (100), which is shown in the second cube.

When the normal points in negative direction along the principal axes, the notation uses a bar above the negative index. The $(\bar{1}\bar{1}1)$ plane has a normal that points in the $-\hat{x} - \hat{y} + \hat{z}$ direction. Note that there is a sign ambiguity in the notation because $(\bar{1}\bar{1}1)$ and $(11\bar{1})$ both describe normals to the same plane pointing in opposite directions. Both forms are acceptable.

The numbers used to describe a plane (hkl) are known as the Miller indices of the plane.

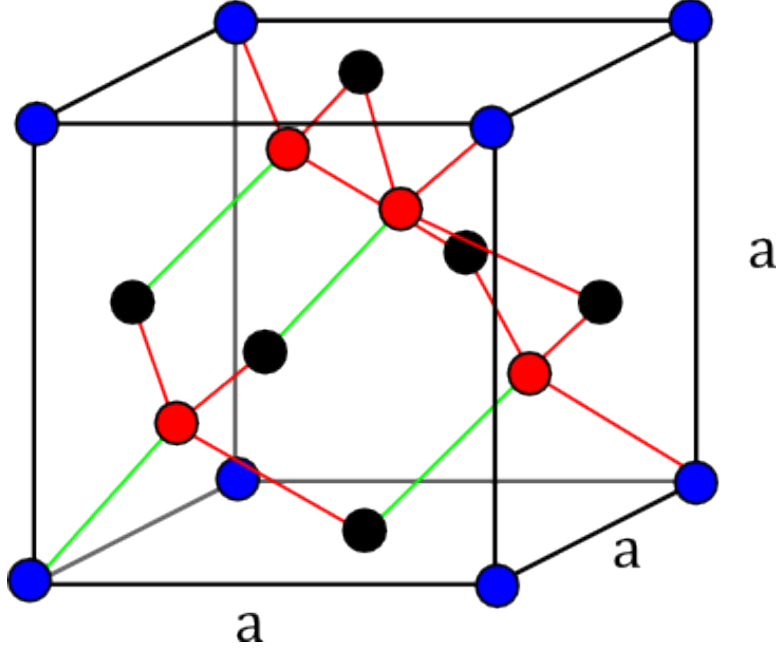


Figure 4: The unit cell for diamond/silicon.

They are used to define the reciprocal lattice vector, $\vec{\tau}$, which is defined as

$$\vec{\tau} = \frac{2\pi}{a}(h\hat{x} + k\hat{y} + l\hat{z}) \quad (1)$$

The magnitude of $\vec{\tau}$ is $\tau = \frac{2\pi}{a}\sqrt{h^2 + k^2 + l^2}$, the unit vector in the direction of $\vec{\tau}$ is $\hat{\tau} = \frac{1}{\sqrt{h^2 + k^2 + l^2}}(h\hat{x} + k\hat{y} + l\hat{z})$. Note that the magnitude of the reciprocal lattice vector is $\tau = \frac{2\pi}{d_{hkl}}$ where d_{hkl} is the distance between the lattice planes (hkl) .

1.1.1 Unit Cell of Diamond-Like Crystals

Silicon and diamond crystals both have the same cubic unit cell that is somewhat more difficult to visualize than the above cubic cells. The diamond unit cell is shown in Figure 4. The underlying structure is FCC, where the blue dots indicate the vertices of the cube, and the black dots are the center points on each of the faces. The red dots are the four additional atoms. Each of the red atoms is a distance $a/4$ in the $\hat{x} + \hat{y} + \hat{z}$ direction relative to points on the underlying FCC structure. The translation necessary to get the red points from the original FCC cell is shown by the green lines.

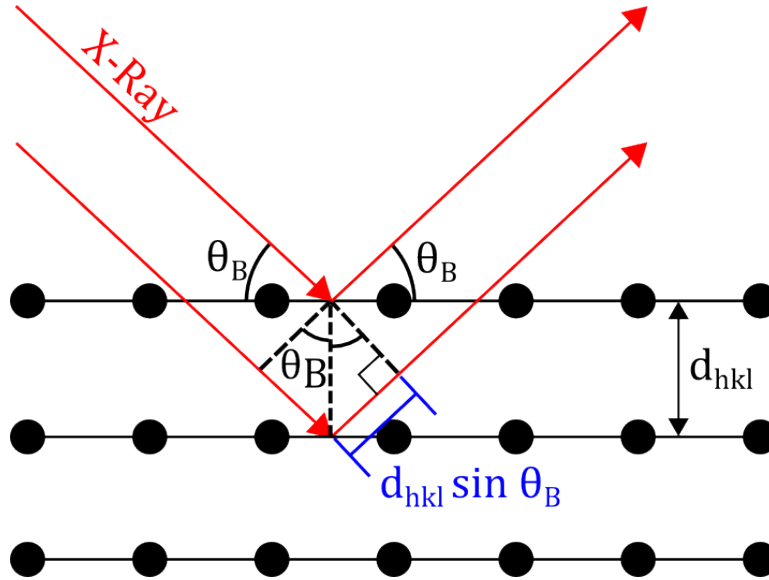


Figure 5: Bragg x-ray reflection.

1.2 Bragg Reflection of X-Rays

1.2.1 X-Ray Crystallography

When x-rays are sent through a crystal, bright spots can be produced at sharp angles relative to the incident x-ray. Bragg discovered that this phenomenon can be described by coherent reflections of the x-rays from crystal planes. The process is shown in Figure 5. The path length difference between x-ray reflections from adjacent crystal planes is $2d_{hkl} \sin \theta_B$ where d_{hkl} is the spacing between crystal planes (hkl) and θ_B is the Bragg angle, the angle of the incident x-ray. When the additional path length is equal to a multiple of the x-ray wavelength, λ , the outgoing rays constructively interfere. This is the condition for Bragg reflection:

$$2d_{hkl} \sin \theta_B = n\lambda \quad (2)$$

We will usually be concerned with the case where $n = 1$. Away from the Bragg angle, the x-rays do not constructively interfere, leading to a localized bright spot at the Bragg angle.

The Bragg model is heuristic, but more sophisticated models give essentially the same results. This model is advantageous because of it is intuitive and simple.

1.2.2 Structure Factors and Forbidden Reflections

A more realistic model models the atoms in the crystal absorbing the x-ray and emitting it isotropically. Where the isotropic emissions constructively interfere are the Bragg "reflections." Occasionally, the arrangement of the atoms in the unit cell can be such that within one unit cell, the re-emitted radiation destructively interferes leaving no opportunity for constructive interference from successive period unit cells.

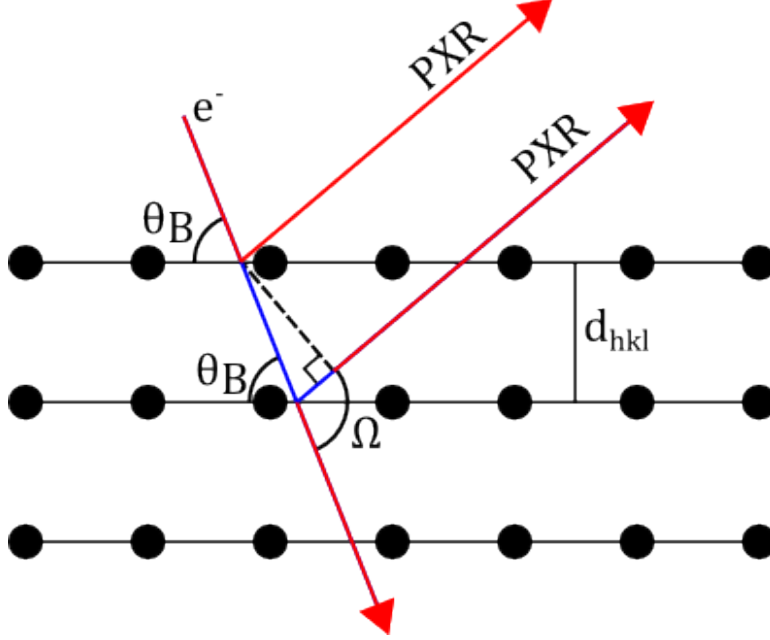


Figure 6: Reflection of virtual photon field from the crystal planes. The electron impacts the crystal at angle θ_B with respect to the crystal planes, and the PXR is emitted at angle Ω with respect to the initial electron velocity.

Such a cancellation is governed by the crystal structure factor. The structure factor depends on the Miller indices of a given plane, and when the structure factor is zero, that reflection is forbidden. Computing the structure factor for various crystals gives selection rules on the Miller indices for allowable x-ray reflections, depending on the geometry of the unit cell.

For Diamond-like unit cells, reflections are allowed if the Miller indices hkl are all odd, or if they are all even, the sum $h + k + l$ must be a multiple of four. Reflections are forbidden if the Miller indices are mixed even and odd, or if they are all even and the sum is not a multiple of four.

1.3 PXR as Reflected Virtual Photons

Parametric x-ray radiation is a kind of Bragg reflection. The electric field of a charged particle is a field of virtual photons of many frequencies. When the charged particle passes through a crystal, those virtual photons that have wavelengths satisfying the Bragg condition can be transformed into real photons and reflected.

In Figure 6, a diagram of PXR is shown. The length of the blue segment must be equal to an integer number of wavelengths for the reflected photons to constructively interfere.

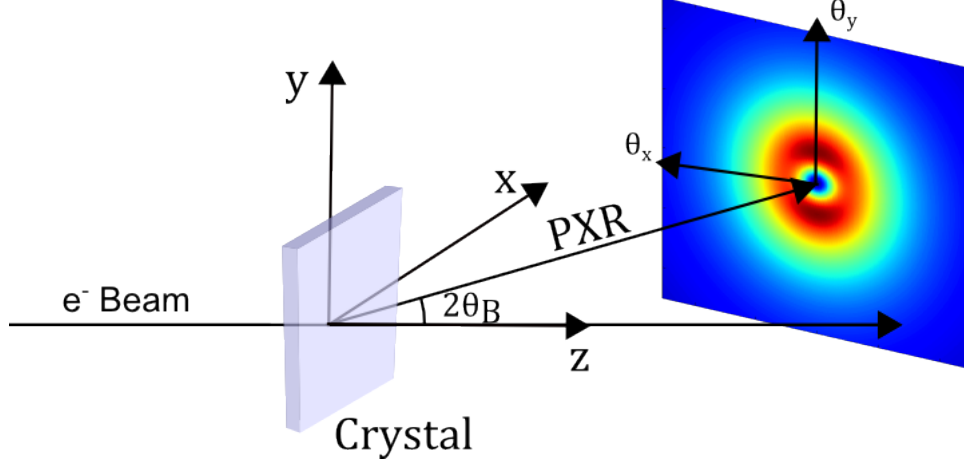


Figure 7: A schematic of the PXR reflection in three dimensions. We pick coordinates such that the center of the PXR distribution is in the xz plane. The red spots correspond to a greater intensity of PXR and the blue spots correspond to less intensity.

The length of the blue path is

$$\frac{d_{hkl}}{\sin \theta_B} + \frac{d_{hkl} \cos(\pi - \Omega)}{\sin \theta_B} = \frac{d_{hkl}}{\sin \theta_B} (1 - \cos \Omega) = n\lambda \quad (3)$$

Because $E = hc/\lambda$, the energy of the PXR can be written

$$E = \hbar c \tau \frac{\sin \theta_B}{1 - \cos \Omega} \quad (4)$$

Therefore, only those photons with energy that satisfies these conditions will be produced. Note that it is possible to measure photons slightly away from the Bragg angle, hence the use of Ω . At exactly the Bragg angle, $\Omega = 2\theta_B$ so that

$$E = \frac{\hbar c \tau}{2 \sin \theta_B} \quad (5)$$

1.4 Shape of PXR Emission

While this reflection treatment accurately calculated the PXR energy, a more sophisticated analysis allows one to calculate the distribution of PXR around the Bragg angle. Ignoring for the moment the magnitude of the PXR at a given angle, the shape of the angular distribution is described by

$$N(\theta_x, \theta_y) = \frac{\theta_x^2 \cos^2 2\theta_B + \theta_y^2}{(\theta_x^2 + \theta_y^2 + \theta_{ph}^2)^2} \quad (6)$$

where θ_x is the angle in the diffraction plane and θ_y is the angle perpendicular to θ_x out of the diffraction plane [11]. These coordinates are shown in Figure 7. The characteristic

angle, θ_{ph} , is given by

$$\theta_{\text{ph}} = \sqrt{\frac{1}{\gamma^2} + \frac{\omega_p^2}{\omega^2}} \quad (7)$$

where γ is the relativistic Lorentz factor of the electron beam, ω_p is the plasma frequency of the crystal, and ω is the frequency of the PXR. Typically, $\theta_{\text{ph}} \approx 1/\gamma$.

The shape of this distribution is also shown in Figure 7 as the color plot. Notice there are two intensity peaks above and below the Bragg angle. These peaks are positioned at $\theta_x = 0$, $\theta_y = \pm\theta_{\text{ph}}$. Also notice that at exactly the Bragg angle, $(\theta_x, \theta_y) = (0, 0)$, there is no PXR. This is a destructive interference effect.

1.5 Magnitude of PXR Emission

The full expression for the magnitude of PXR at a given angle is given by

$$\begin{aligned} \frac{d^2 N}{d\theta_x d\theta_y} &= \frac{\alpha}{4\pi} \frac{\omega_B}{c \sin^2 \theta_B} \left[L_a \left| \frac{\hat{n} \cdot \hat{\Omega}}{\hat{n} \cdot \hat{v}} \right| \left(1 - e^{-t/(L_a |\hat{n} \cdot \hat{\Omega}|)} \right) \right] \chi_g^2 e^{-2W} N(\theta_x, \theta_y) \\ &= N_0 N(\theta_x, \theta_y) \end{aligned} \quad (8)$$

where α is the fine-structure constant, ω_B is the frequency of PXR at the Bragg angle, the term in square brackets is the ‘‘geometric factor’’, χ_g^2 is the square of the Fourier transform of the electric susceptibility, e^{-2W} is the Debye-Waller factor, and $N(\theta_x, \theta_y)$ is given by equation 6 [11].

1.5.1 The Geometric Factor

The geometric factor in equation 8 is given by

$$f_{\text{geo}} = L_a \left| \frac{\hat{n} \cdot \hat{\Omega}}{\hat{n} \cdot \hat{v}} \right| \left(1 - e^{-t/(L_a |\hat{n} \cdot \hat{\Omega}|)} \right) \quad (9)$$

where L_a is the attenuation length of x-rays of a given energy in the material, \hat{n} is the normal to the crystal surface through which the electron beam passes, $\hat{\Omega}$ is the emission direction of the PXR, \hat{v} is the direction of the velocity of the electron beam, and t is the crystal thickness [10]. The attenuation lengths L_a can be found from online databases [4].

This term represents two pieces of physics. First the amount of PXR produced per unit length as the electron traverses the crystal is constant; therefore, the greater the length of crystal the electron traverses, the more PXR there will be. On the other hand, the x-rays are attenuated as they leave the crystal. PXR that must traverse through the entire crystal will contribute significantly less than PXR produced at the surface of the crystal. The geometric factor f_{geo} is derived by integrating the attenuation factor over the path of the electron in the crystal.

The dot products in f_{geo} depend on the Bragg angle and the cut of the crystal with respect to the reflecting planes. If the reflecting planes are parallel to the crystal surface,

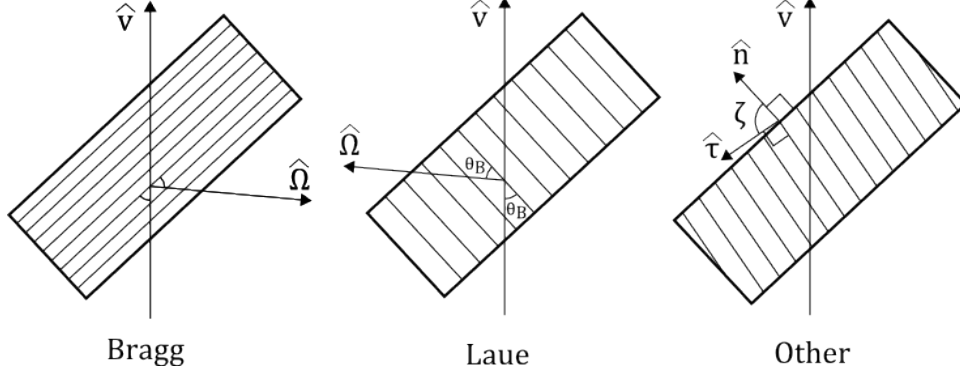


Figure 8: The different ways a crystal can be cut with respect to the reflecting crystal plane. $\hat{\Omega}$ is the direction of the reflected PXR, \hat{n} is the unit normal to the surface of the crystal, $\hat{\tau}$ is the normalized reciprocal lattice vector, and \hat{v} is the direction of the velocity of the electron beam.

then the crystal is said to have a Bragg cut. If they are perpendicular, they crystal is cut in the Laue geometry. Of course, it is possible to cut the crystal planes at some other angle with respect the surface. In this case, ζ is the angle between the normal to the crystal surface and the normal to the crystal planes and is defined to be in the range $0 \leq \zeta \leq \pi/2$.

In the Bragg geometry, the PXR is always reflected through the entry surface, and in the Laue geometry, PXR is always reflected through the exit surface. In other geometries, the PXR can be reflected in either direction depending on the Bragg angle. When PXR is reflected perpendicular to \hat{n} , $f_{\text{geo}} = 0$, since the crystal is infinite in that direction and all the PXR is absorbed in the crystal.

The general expression for f_{geo} in terms of ζ and θ_B is

$$f_{\text{geo}} = L_a \left| \frac{\sin(\zeta - \theta_B)}{\sin(\zeta + \theta_B)} \right| \left[1 - \exp\left(\frac{-t}{L_a |\sin(\zeta - \theta_B)|}\right) \right] \quad (10)$$

Note that when $\zeta = \theta_B$, $f_{\text{geo}} = 0$. This corresponds to the condition that the PXR is reflected entirely entirely along the longer dimensions of the crystal. Note also that $f_{\text{geo}} \leq L_a$ with equality only when $t = \infty$ and $\zeta = 0, \pi/2$ (Bragg/Laue geometry).

1.5.2 Fourier Transform of the Electric Susceptibility (χ_g)

The factor χ_g^2 accounts for the efficiency with which photons are diffracted in the crystal. It can be computed from

$$\chi_g^2 = \frac{\lambda^4 r_e^2}{\pi^2 V_c^2} S_{hkl}^2 [(f_0 + f_1 - Z)^2 + f_2^2] \quad (11)$$

where λ is the x-ray wavelength, r_e is the classical electron wavelength, V_c is the volume of the crystal unit cell, S_{hkl} is the structure factor, Z is the atomic number, and f_0 , f_1 , and f_2 are the atomic form factors [11]. The factors f_1 and f_2 are relatively small correction terms

that can be found in online databases [4], and f_1 can be computed from the Cromer-Mann coefficients by

$$f_0 = c + \sum_{i=1}^4 a_i e^{-b_i s^2} \quad (12)$$

where $s = \frac{\sin \theta_B}{\lambda}$ and a_i , b_i , and c are the Cromer-Mann coefficients which can be found in online tables [9].

For diamond-like crystals, the structure factor $S_{hkl}^2 = 32$ if the Miller indices are odd, or $S_{hkl}^2 = 64$ if the Miller indices are even (and sum to a multiple of four).

Since $\lambda \propto 1/E$, the χ_g^2 factor has a roughly $1/E^4$ dependence on energy. Additionally, f_0 contains terms of the form e^{-E^2} . Both of these dependencies limit the production of PXR at high energies. The energy dependence of these and other parameters can be found in the Appendix.

1.5.3 Debye-Waller Factor

The Debye-Waller factor accounts for disruptive effects of thermal lattice vibrations. At room temperature, this factor will usually be close to one. For example, in diamond at room temperature, it amounts to a factor of 0.9825. The term is given by

$$e^{-2W} = e^{-\tau^2 u^2(T)} \quad (13)$$

where τ is the reciprocal lattice vector. $u^2(T)$ is given by

$$u^2(T) = \frac{3\hbar}{4Ak_B T_D} \left(1 + 4 \frac{T^2}{T_D^2} \int_0^{T_D/T} \frac{y dy}{e^y - 1} \right) \quad (14)$$

where A is the atomic mass number, k_B is Boltzmann's constant, T_D is the crystal's Debye temperature, and y is simply an integration variable.

2 Simulated Angular Distribution

Equation 8 is the distribution of PXR assuming ideal conditions. That is, every electron in the beam hits the crystal at the same point at the same angle, the electrons continue on exactly this course through the crystal, all PXR is assumed to come from the same point, and the crystal planes are all perfectly parallel. In order for the simulation to accurately predict how many photons a detector would measure, it is necessary to understand these effects.

2.1 Multiple Scattering

Among the largest of these effects for electron beams with energies in the tens of MeV is electron multiple scattering in the crystal. the electrons are slightly scattered off their

initial trajectory by colliding with atoms in the material. The scatters cause the electron to undergo a kind of random walk, and after traveling a distance x into the material, the electron will be traveling at an angle θ_{ms} relative to its initial linear trajectory. The angle θ_{ms} is approximately Gaussian distributed with a standard deviation given by

$$\sigma_{\theta_{\text{ms}}} = \frac{13.6\text{MeV}}{\beta cp} \sqrt{\frac{x}{X_0}} \left[1 + 0.038 \ln \left(\frac{x}{X_0} \right) \right] \quad (15)$$

where βc is the electron velocity, p is its momentum, x is the distance into the material, and X_0 is the radiation length of the material [5]. The radiation length is the length scale of energy loss of particles traveling through matter. It is given by

$$\frac{1}{X_0} = 4\alpha r_e^2 \frac{N_A}{A} \{ Z^2 [L_{\text{rad}} - f(Z)] - Z L'_{\text{rad}} \} \quad (16)$$

where α is the fine-structure constant, r_e is the classical electron radius, N_A is Avogadro's number, A is the atomic weight of the material, Z is the atomic number of the material, and for $Z > 4$, $L_{\text{rad}} = \ln(184.15Z^{-1/3})$ and $L'_{\text{rad}} = \ln(1194Z^{-2/3})$. For $Z \leq 4$, L_{rad} and L'_{rad} are given by a table [5]. Additionally,

$$f(Z) = a^2 \left[(1 + a^2)^{-1} + 0.20206 - 0.0369a^2 + 0.0083a^4 - 0.002a^6 \right]$$

where $a = \alpha Z$.

2.1.1 Convolution

The multiple scattering of the electron changes the angle the electron impacts the crystal planes and therefore on each scatter, the angular distribution is centered on a different location. A first order method to understand this effect is to convolve the multiple scattering Gaussian with the already known angular distribution. The new angular distribution would then be given by

$$\begin{aligned} \Lambda(\theta_x, \theta_y) &= A_{\text{norm}} \iint_{-2\sigma_\theta}^{2\sigma_\theta} \frac{d^2 N}{d\theta_x d\theta_y}(\theta_x - q_x, \theta_y - q_y) \times e^{\frac{-q_x^2 - q_y^2}{2\sigma_\theta^2}} dq_x dq_y \\ &= A_{\text{norm}} \times N_0 \iint_{-2\sigma_\theta}^{2\sigma_\theta} \frac{(\theta_x - q_x)^2 \cos^2 2\theta_B + (\theta_y + q_y)^2}{[(\theta_x - q_x)^2 + (\theta_y - q_y)^2 + \theta_{\text{ph}}^2]^2} \times e^{\frac{-q_x^2 - q_y^2}{2\sigma_\theta^2}} dq_x dq_y \end{aligned} \quad (17)$$

The σ_θ used is that for multiple scattering through the entire thickness of the crystal. The normalization factor A_{norm} is chosen to preserve the total area under the curve after the convolution:

$$\iint_{-2\sigma_\theta}^{2\sigma_\theta} \Lambda(\theta_x, \theta_y) d\theta_x d\theta_y = \iint_{-2\sigma_\theta}^{2\sigma_\theta} \frac{d^2 N}{d\theta_x d\theta_y}(\theta_x, \theta_y) d\theta_x d\theta_y \quad (18)$$

The limits in these integrals should be $\pm\infty$; however, beyond $2\sigma_\theta$, the integrand is approximately zero. The shorter range is more convenient when computing this integral numerically.

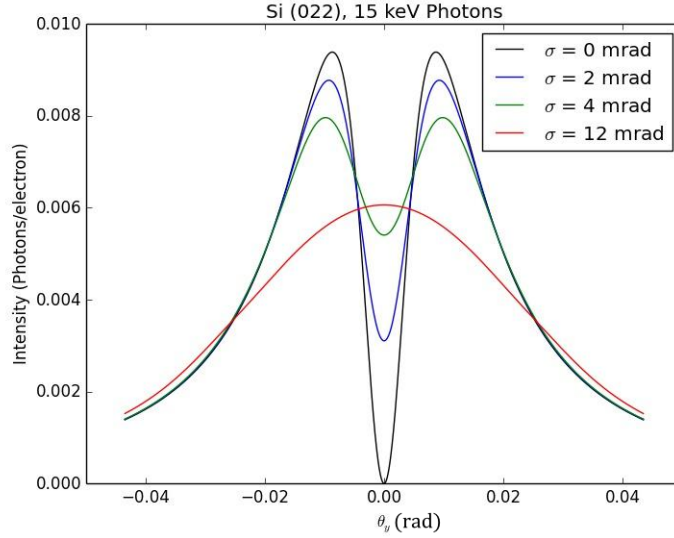


Figure 9: The effect of multiple scattering on the angular distribution along θ_y , with $\theta_x = 0$.

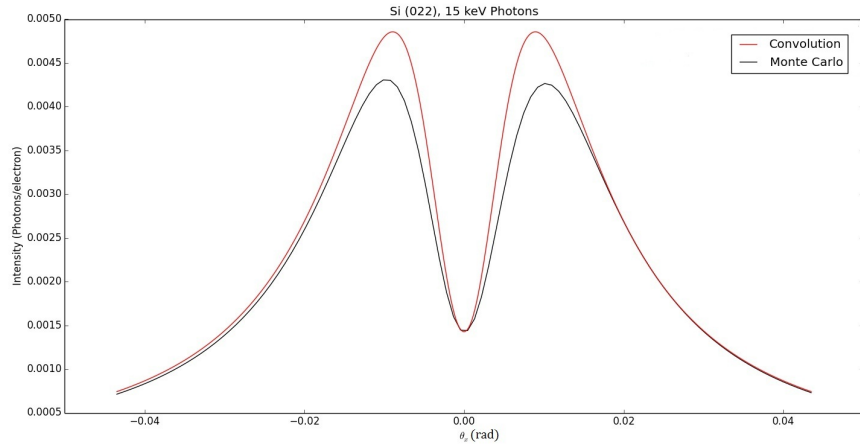
Note that in equation 17, N_0 is pulled out of the integral even though it has a dependence on the angle through its dependence on E . The value for the energy used in computing N_0 is the PXR energy at the Bragg angle. This removes a slight asymmetry that would otherwise develop.

The effect of this convolution is shown in Figure 9, a plot of the intensity distribution vs θ_y where $\theta_x = 0$. When σ_θ is low, the two peaks are visible and at $\theta_y = 0$, there is no light, as expected. When σ_θ increases, the minimum becomes filled in as the magnitude of the peaks decreases, preserving the area under the curve. At large σ , the double peak structure disappears completely, leaving a single peak in the center.

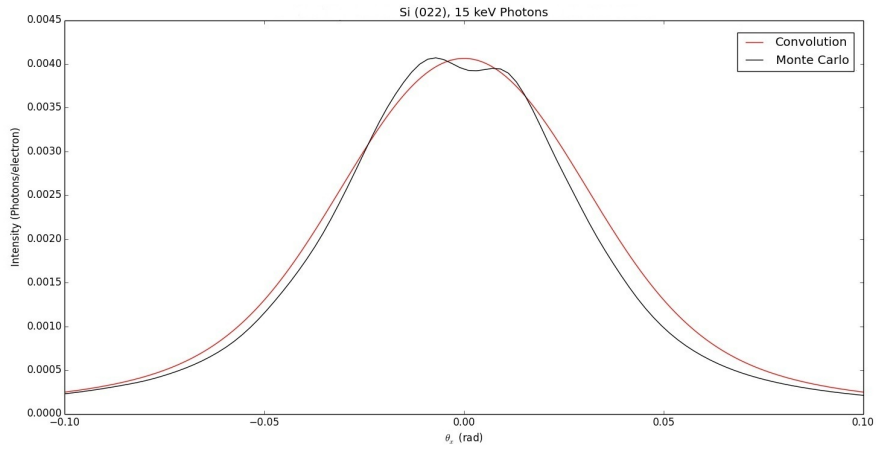
2.1.2 Monte Carlo

A more accurate method to compute the angular distribution is to use a Monte Carlo of electron multiple scattering in the crystal, though the results are quite close to that of the convolution. The Monte Carlo uses a specified number of steps through the crystal, and at each step it updates the total multiple scattering angle, α . The amount by which α is changed is sampled from the multiple scattering Gaussian through a thickness of crystal equal to the step size. I then compute the new $\frac{d^2N}{d\theta_x d\theta_y}$ based on on the the updated α . This distribution is added to those from the previous steps, but shifted from center by an angle α . This is what causes the smearing effect.

One complication arises in the geometric factor f_{geo} because it is obtained from integrating the attenuation through the entire length of the crystal. Instead, I use a “local” geometric factor that accounts for attenuation at a particular depth z into the crystal. This geometric



(a) $\sigma_\theta = 2$ mrad.



(b) $\sigma_\theta = 12.3$ mrad.

Figure 10: A comparison of the multiple scattering analysis with Monte Carlo (black) and convolution (red) for different σ_θ . The σ_θ reported is that for multiple scattering through the entire thickness of the crystal.

factor is given by

$$f_{\text{geo}} = \Delta z e^{-l(z)/L_a} \quad (19)$$

where Δz is the step size and $l(z)$ is the escape length of the PXR from location z . For general crystal geometries, the escape length is given by

$$l(z) = \begin{cases} \frac{t - z \sin(\theta_B + \zeta)}{\sin(\zeta - \theta_B)} & \theta_B < \zeta \\ z \frac{\sin(\theta_B + \zeta)}{\sin(\theta_B - \zeta)} & \theta_B \geq \zeta \end{cases} \quad (20)$$

where ζ is the angle between the reciprocal lattice vector and the normal to the crystal surface, as before, and t is the crystal thickness. When $\theta_B < \zeta$, the PXR is reflected out the surface through which the electron entered, and when $\theta_B > \zeta$, the PXR is reflected out the surface through which the electron exits. When $\theta = \zeta$, the PXR is reflected along the infinite direction of the crystal and $l(z) = \infty \implies f_{\text{geo}} = 0$.

As shown in Figure 10, the agreement between the Monte Carlo and the convolution is rather good for different values of σ_θ . Notice that an asymmetry does develop in the Monte Carlo when the multiple scattering is large. This is because in the Monte Carlo, the dependence of N_0 on the scattering angle is included. The value of N_0 used for each step is the value at the Bragg angle for that step.

2.2 Other Anomalous Contributions

While multiple scattering causes the largest change in the shape of the angular distribution, other approximations are made. Several of them have been considered and determined to be negligible. In particular, beam divergence at the crystal on the order of a few milliradians has been included in the Monte Carlo and found to have essentially no effect. The multiple scattering, on the order of tens of milliradians through typical crystals dominates over beam divergence, unless the beam divergence is very large.

The fact that PXR is emitted from different depths in the crystal also has little effect. If a detector is distance d away, the angular size of the crystal projected onto the detector at angle θ_B is $\theta_t = \tan^{-1}(\frac{t}{d} \sin \theta_B)$. This geometry is shown in Figure 11a. If we set the parameters to typical values, $\theta_B = \frac{\pi}{4}$, $t = 1$ mm, and $d = 1$ m, then $\theta_t = 0.041^\circ$. On the other hand, the cone of PXR has a characteristic size $1/\gamma$, which for a 50 MeV beam is 0.57° , an order of magnitude larger than θ_t . Thus the PXR emitted from the front of the crystal can be assumed to center on the same point as PXR emitted from the back of the crystal. If the beam energy were higher by about an order of magnitude, then this effect would be important.

Finite beam spot size on the crystal has a similar geometry to affects from crystal thickness. If the diameter of the beam is s , this corresponds to an angular spread on the detector of $\theta_s = \tan^{-1}(\frac{s}{d} \cos \theta_B)$. This geometry is shown in Figure 11b. If $s/d \ll 1/\gamma$, the effect of beam spot size is minimal.

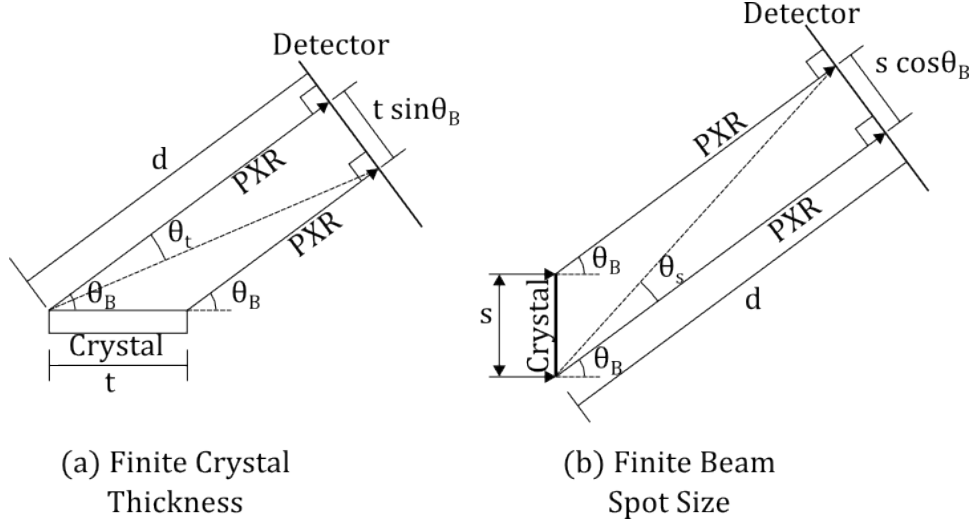


Figure 11: The geometry of crystal thickness and beam spot size.

Lastly, crystal mosaicity, the fact that the atoms of the crystal are not all perfectly aligned, has not been considered. We could assume that crystal mosaicity causes some random Gaussian deviation of the reciprocal lattice vectors around the central direction. In this case, the effect of crystal mosaicity will be similar to that of multiple scattering. However, if the standard deviation of the angle of the reciprocal lattice vectors is significantly less than the standard deviation in angles for multiple scattering, then crystal mosaicity would not be a significant effect in comparison.

2.3 Computing Yield into a Detector

Once the angular distribution of the PXR yield is understood, it can be used to compute the number of photons observed in a detector. To do this, I integrate the angular distribution, convolved with the multiple scattering Gaussians, over the area of the detector, which I assume to be rectangular. If the detector has sides of length Δx and Δy and is placed a distance R from the crystal, then the number of photons per electron seen by the detector is

$$N = \int_{-\Delta y/2R}^{\Delta y/2R} \int_{-\Delta x/2R}^{\Delta x/2R} \Lambda(\theta_x, \theta_y) d\theta_x d\theta_y \quad (21)$$

Since the multiple scattering Monte Carlo is rather close to the convolved distribution, using the convolution is sufficiently accurate. Multiplying N by the electron flux (number of electrons per second) of the beam will give the prediction for the number of photons observed per second. Combined with the average energy per photon computed from the geometry of the experiment, the power on the detector can be computed, a critical experimental parameter.

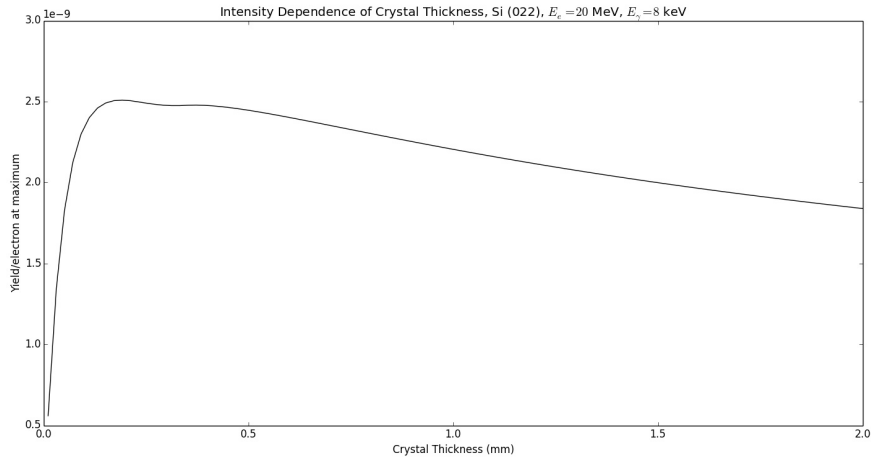


Figure 12: The dependence of the measured number of photons per electron on the thickness of the crystal.

2.3.1 Yield vs Crystal Thickness

An interesting dependency to examine is how the yield into a detector varies with the thickness of the crystal. An example of this calculation is plotted in Figure 12. The detector is assumed to always be centered on the maximum of the angular distribution. The plot shows initial rise, a plateau, then a slow decline. The initial rise is due entirely to the geometric factor. Since a constant amount of PXR is produced per unit length, the thicker crystal causes a greater production of PXR. When the crystal thickness reaches the order of the attenuation length of the x-rays, then the growth of the geometric factor slows down, as PXR produced deep in the crystal is attenuated before it can escape. As the crystal thickness goes to infinity, the geometric factor asymptotes to its maximum value and effectively becomes constant.

The gradual decrease is when the crystal is thick enough that multiple scattering becomes an important issue. After the geometric factor maximizes, the number of photons produced into all angles is essentially constant as the thickness increases. However, the multiple scattering smears out the distribution, lowering the number of photons into the angle spanned by the detector.

The plateau is after the geometric factor reaches its maximum and before multiple scattering becomes significant. When designing the experiment, it is best to have a crystal with a thickness near this plateau.

2.3.2 Yield vs PXR Energy

Another interesting dependency is how the yield depends on photon energy. In this case, a thin crystal is used and multiple scattering is ignored, for computational efficiency. As before,

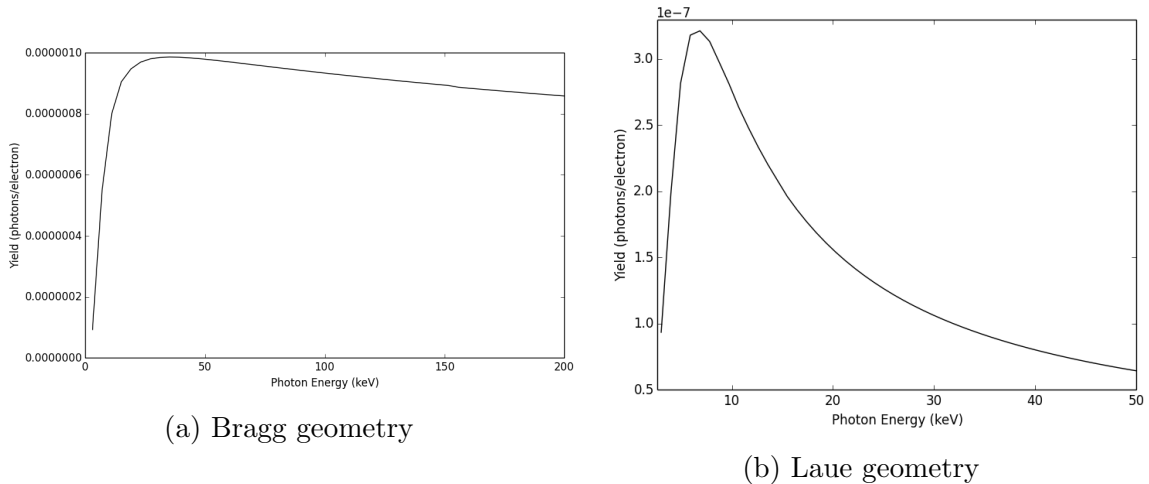


Figure 13: The dependence of the number of photons per second on the PXR energy. The parameters of this simulation were: a diamond crystal, PXR from the (111) plane, crystal thickness of $168 \mu\text{m}$, electron beam energy of 50 MeV, detector placed 1 m from crystal, and a detector size of $1 \text{ cm} \times 1 \text{ cm}$.

the detector is assumed to always be centered on a maximum of the angular distribution. A plot of the result is shown in Figure 13. Interestingly, the shape of the plot depends strongly on the cut of the crystal. In both plots, there is a sharp initial rise. This is due to two effects in Equation 8, the angular yield equation. First, there is a factor of $\omega_B / \sin^2 \theta_B$. Since $\omega_B \propto E$ and $1 / \sin \theta_B \propto E$, this factor is proportional to E^3 . Additionally, though less significantly, low energy x-rays suffer greater attenuation than higher energy x-rays.

After the initial rise, in the Bragg geometry the yield gradually decreases out to large energies. The decrease is due to the χ_g^2 which decreases sharply at high energies, see Figure 20 in the Appendix. The decrease is not more steep because at large energies, the Bragg angle is small, and when the Bragg angle is small in the Bragg geometry, the electron impacts the crystal at shallow angles and is in the crystal for large distances. At 200 keV PXR and a crystal thickness of $100 \mu\text{m}$, the electron travels through 6.6 mm of crystal. Additionally, the x-rays have a large attenuation length at large energies, making f_{geo} large, and the E^3 factor also grows rapidly. Lastly, at large energies χ_g^2 is very small but relatively slowly decreasing compared to how rapidly it decreases at low energies. All these factors combine to keep the yield only slowly decreasing.

Note that multiple scattering, which is ignored in this calculation, does become significant when the electron is traversing millimeters of crystal. This effect would cause the decrease to be steeper than in the plot. Also, it would be experimentally impractical to use this high energy PXR because at 200 keV, the Bragg angle is 0.86° , which implies the PXR is nearly in the same direction as the beam.

In Laue geometry, on the other hand, the electron traverses the minimum amount of crystal when at small Bragg angles. This causes the geometric factor to be unable to counter

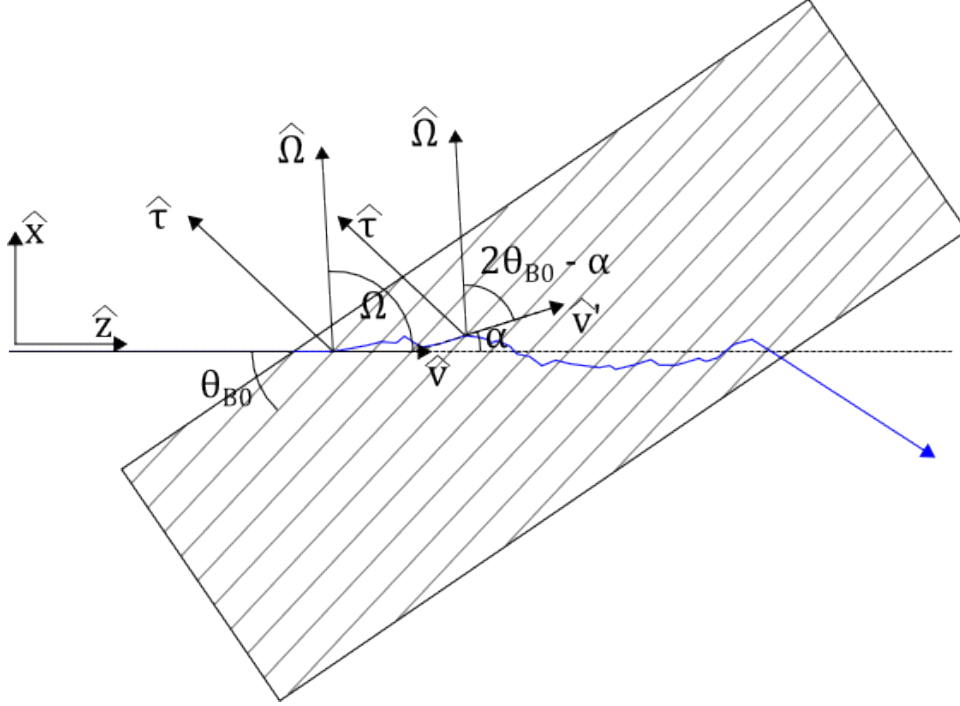


Figure 14: The geometry of electron multiple scattering in the crystal.

the rapid decrease of χ_g^2 , and the yield much more rapidly falls off.

3 Linewidth

The theory of PXR states that the natural linewidth is on the order of millielectronvolts [3]. Such a natural linewidth, however, is difficult to observe because several factors increase it significantly. In particular multiple scattering and a finite detector size will increase the measured linewidth.

3.1 Multiple Scattering

When an electron with velocity \hat{v} passes through a crystal with reciprocal lattice vector in direction $\hat{\tau}$ and the PXR is observed in direction $\hat{\Omega}$, the energy of the PXR is

$$E = \hbar c \tau \frac{|\hat{v} \cdot \hat{\tau}|}{1 - \hat{v} \cdot \hat{\Omega}} \quad (22)$$

where equation 4 has been rewritten using dot products. We will consider multiple scattering in a plane with a fixed observation location in direction $\hat{\Omega}$. When the electron undergoes multiple scattering, the velocity vector shifts $\hat{v} = \hat{z} \rightarrow \hat{v}' = \hat{z} \cos \alpha + \hat{x} \sin \alpha$. Additionally,

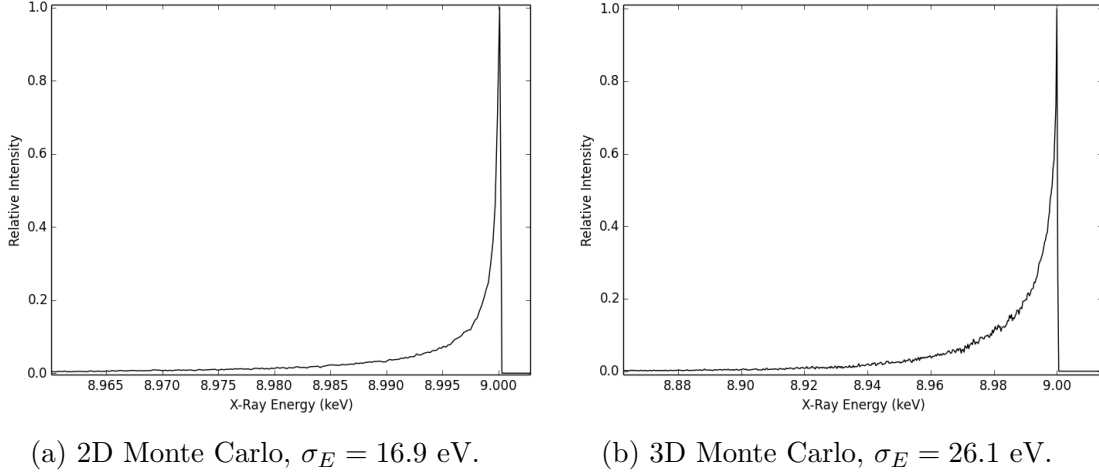


Figure 15: The Monte Carlo energy spectra in two and three dimensions accounting for only multiple scattering. Both simulations used the same input parameters. The crystal was a $168 \mu\text{m}$ thick diamond crystal in the Bragg geometry with PXR from the (111) plane and a beam energy of 20 MeV.

we know $\hat{\tau} = -\hat{z} \sin \theta_{B0} + \hat{x} \cos \theta_{B0}$ and $\hat{\Omega} = \hat{z} \cos 2\theta_{B0} + \hat{z} \sin 2\theta_{B0}$. Using equation 22, the energy for PXR from the scattered electron is

$$E = \hbar c \tau \frac{\sin(\theta_{B0} + \alpha)}{\sin^2(\theta_{B0} + \alpha/2)} \quad (23)$$

This expression for energy has the interesting feature that it is maximal when $\alpha = 0$, which implies that any multiple scattering will reduce the observed energy.

Using equation 23, it is simple to write a Monte Carlo to find the distribution of energies. The electron is stepped through the crystal using a fixed step size, and after each step, a change in angle is picked from a Gaussian with standard deviation given by equation 15. Then the energy is computed with this new angle. The energies are not simply histogrammed, however, because not all energies are produced from the crystal equally. To account for this, for each energy, I calculated a weight given by the energy dependent terms in equation 8. The weight is the product of E^3 , equation 19, and χ_g^2 . This weight is then added to whichever bin is determined by the energy.

The result is shown in Figure 15(a). Since the average value of α is zero, the peak of the energy spectrum is at 9 keV, which is the energy of the PXR without multiple scattering.

3.1.1 Three Dimensions

A more sophisticated approach uses multiple scattering in three dimensions. To do the three dimensional Monte Carlo, at each step I rotate the unit velocity vector \hat{v} about an arbitrarily determined line perpendicular to \hat{v} to get the vector \hat{v}' . As before, the angle of rotation is

determined by sampling from the multiple scattering Gaussian. However, because the angle for multiple scattering in a plane is the projection of this 3D scattering, the angle used in the 3D Monte Carlo is greater than that for the 2D case by a factor of $\sqrt{2}$ [5]. After this first rotation, I then rotate \hat{v}' around \hat{v} by an angle sampled from a uniform distribution between 0 and 2π to get \hat{v}'' . Using \hat{v}'' , I then compute the PXR energy for this step using equation 22. Each energy is weighted as before. The result is shown in Figure 15(b). The spectrum has the same qualitative shape as the 2D Monte Carlo, but it is somewhat wider.

The rotations are accomplished using the Rodrigues rotation matrix, which rotates a vector through angle ψ about the unit vector $\hat{\omega} = (\omega_x, \omega_y, \omega_z)$. The matrix is given by

$$R_{\hat{\omega}}(\psi) = \begin{pmatrix} \cos \psi + \omega_x^2 \xi & -\omega_z \sin \psi + \omega_x \omega_y \xi & \omega_y \sin \psi + \omega_x \omega_z \xi \\ \omega_z \sin \psi + \omega_x \omega_y \xi & \cos \psi + \omega_y^2 \xi & -\omega_x \sin \psi + \omega_y \omega_z \xi \\ -\omega_y \sin \psi + \omega_x \omega_z \xi & \omega_x \sin \psi + \omega_y \omega_z \xi & \cos \psi + \omega_z^2 \xi \end{pmatrix} \quad (24)$$

with $\xi = 1 - \cos \psi$ [2].

3.2 Detector Size

Another important factor for the measured linewidth is the size of the detector being used to measure the linewidth. Since any finite-sized detector spans a range of angles, it also spans a range of energies, increase the measured energy spread. This effect can be added to the planar multiple scattering Monte Carlo. At each step, the energy is computed for a range of angles corresponding to the angles spanned by the detector. Let ϕ be the angular parameter that sweeps over the detector each step through the crystal. The range of ϕ is $-\frac{1}{2}\Delta\theta_D \leq \phi \leq \frac{1}{2}\Delta\theta_D$ where $\Delta\theta_D$ is the angular size of the detector. Then, similar to equation 23,

$$E = \hbar c \tau \frac{\sin(\theta_{B0} + \alpha)}{\sin^2(\theta_{B0} + \phi/2 + \alpha/2)} \quad (25)$$

Like before, the energy is weighted, but the weighting is now more complex. The detector spans a relatively large range of angles, so the angular distribution of the PXR can become important. If the detector happens to encompass a peak of the angular distribution, then the energies corresponding to that peak will be more intense. The weight factor w used for energy E is now

$$w = E^3 e^{-l(z)/L_a(E)} \chi_g^2(E) \frac{(\phi + \alpha)^2 \cos^2(2\theta_{B0} + 2\alpha)}{[(\phi + \alpha)^2 + \theta_{\text{ph}}^2]^2} \quad (26)$$

where $l(z)$ is given by equation 20. The dependence of the parameters on energy has been explicitly written. Since the Monte Carlo assumes scattering in the xz-plane, I set $\theta_y = 0$ in the angular distribution. The angular distribution was not needed in the weight factor before because $\phi = 0$ and $\alpha \approx \text{const}$, so the factor was relatively constant.

The result of this computation is shown in figure 16. The narrow, sharp peak of Figure 15 is now significantly wider.

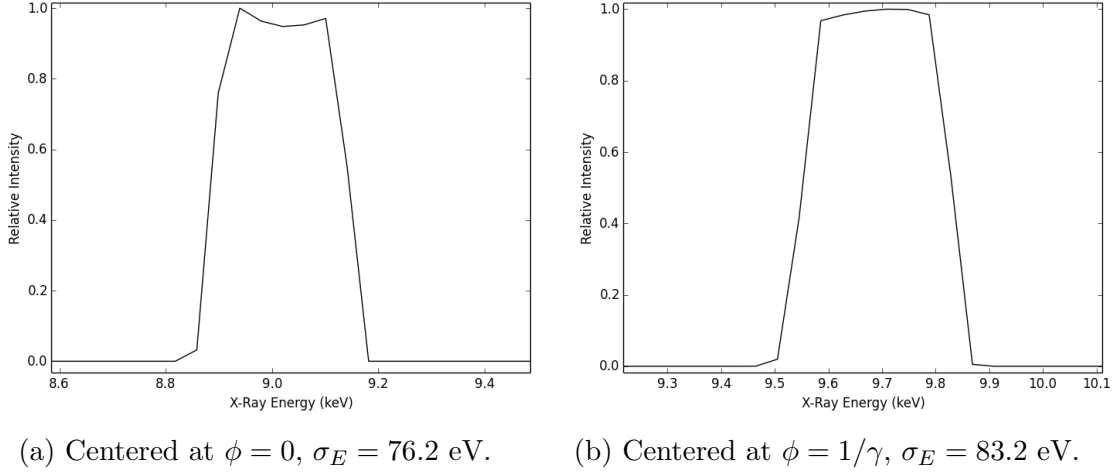


Figure 16: The energy spectrum observed by a detector with finite angular size. The detector was 1 cm across, 1 meter from the crystal. In figure (a), the detector is centered on the Bragg angle and the range of ϕ is $-\frac{1}{2}\Delta\theta_D \leq \phi \leq \frac{1}{2}\Delta\theta_D$. In figure (b), the detector is centered by an angle $1/\gamma$ away from the Bragg angle, and the range of ϕ is $-\frac{1}{2}\Delta\theta_D + 1/\gamma \leq \phi \leq \frac{1}{2}\Delta\theta_D + 1/\gamma$. The parameters of the simulation were the same as in Figure 15. The detector was 1 cm \times 1 cm, placed 1 m from the crystal.

4 PXR while Channeling

Electron channeling in crystal is the phenomenon by which electrons traveling through the crystal are confined between two parallel crystal planes. Because of the periodicity of the atoms in the crystal, the electron oscillates when channeling. This oscillation produces channeling radiation in the direction of motion of the electron. This channeling radiation could be another useful source of x-rays. When studying channeling radiation, it may be desirable to study PXR at the same time, with the same crystal.

At the channeling experiments at the Advanced Superconducting Test Accelerator (ASTA), channeling will be along the (110) plane of diamond. While channeling parallel to this plane, what plane is best to simultaneously produce PXR? We must have the PXR reflected through available windows in the apparatus, which are at 90 degrees transverse to the beam on either side of the beam. We also would like to maximize the energy and the intensity of the PXR.

4.1 $(\bar{1}\bar{1}1)$ Plane

First, I will calculate the characteristics of the PXR when the crystal is perpendicular to the beam and the electron is channeling along the (110) plane. We will use crystal coordinates so that the reciprocal lattice vector can read off from the Miller indices of the plane (note this is a change of coordinate systems from earlier). See figure 17 for how the coordinates are related to the experimental setup.

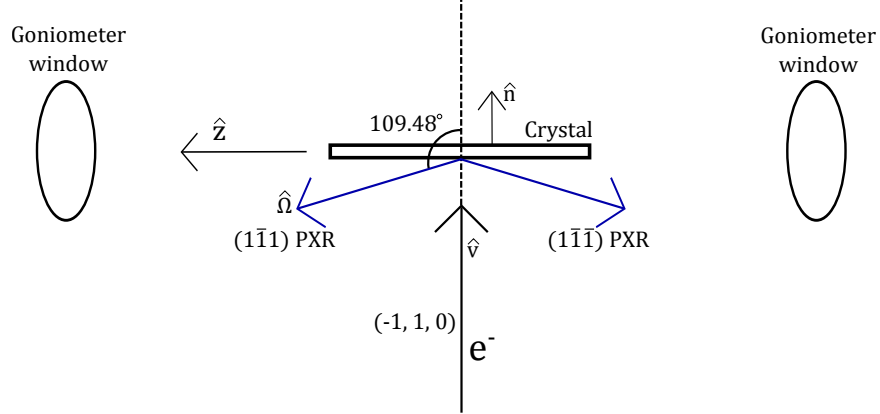


Figure 17: A diagram of the experimental geometry. The channeling planes (110) are parallel to the face of the crystal shown in the diagram. That is, the normal to the channeling planes points out of the page. Since this vector points in the $(1, 1, 0)$ direction, it also defines the x and y axes. They each point 45° upwards above the plane of the page.

In this setup, the unit normal to the channeling crystal planes (the normalized reciprocal lattice vector) is $\frac{1}{\sqrt{2}}(1, 1, 0)$. The unit normal to the surface of this crystal is $\hat{n} = \frac{1}{\sqrt{2}}(-1, 1, 0)$. The velocity of the electrons is parallel to the unit normal to the surface of the crystal, so the unit vector in the direction of the velocity of the electrons is $\hat{v} = \hat{n} = \frac{1}{\sqrt{2}}(-1, 1, 0)$.

Given these coordinates, the direction of the reciprocal lattice vector of the reflecting PXR plane can be immediately determined from the Miller indices. For the $(1\bar{1}1)$ plane, the unit reciprocal lattice vector is $\hat{\tau} = \frac{1}{\sqrt{3}}(1, -1, 1)$.

4.1.1 Bragg Angle

The Bragg angle can be determined from the dot product of $\hat{\tau}$ and \hat{v} from

$$|\hat{\tau} \cdot \hat{v}| = \sin \theta_B \quad (27)$$

The absolute value indicates that θ_B is defined to always be positive. Taking the dot product of the above vectors gives $\sin \theta_B = \sqrt{\frac{2}{3}} \implies \theta_B = 0.9553 \text{ rad} = 54.74^\circ$. This means the PXR will be observed at $2\theta_B = 109.48^\circ$ with respect to the velocity of the beam. It is reflected somewhat backwards, and from the geometry it can be seen that it will also reflect toward $+\hat{z}$ in the current crystal orientation.

The energy of this PXR can be obtained from equation 22. Substituting the parameters for diamond,

$$E = (1.738 \text{ keV}) \frac{\sqrt{h^2 + k^2 + l^2}}{\sin \theta_B} \quad (28)$$

At the Bragg angle of 54.74° , the energy of the PXR is $E = 3.687 \text{ keV}$.

4.1.2 Intensity

As a measure of the intensity, I calculate

$$N_0 = \frac{\alpha}{4\pi} \frac{E}{\hbar c \sin^2 \theta_B} f_{geo} \chi_g^2 \quad (29)$$

which is the factor that gives the amplitude of the intensity distribution, equation 8. f_{geo} is given by equation 9, which requires knowing $\hat{\Omega}$, the direction of the emitted PXR. Since $\hat{\Omega}$ is the reflection of \hat{v} about $\hat{\tau}$, it can be shown that

$$\hat{\Omega} = 2(\hat{v} \cdot \hat{\tau})\hat{\tau} - \hat{v} \quad (30)$$

which implies

$$|\hat{n} \cdot \hat{\Omega}| = |\hat{n} \cdot \hat{v} - 2(\hat{v} \cdot \hat{\tau})(\hat{n} \cdot \hat{\tau})| \quad (31)$$

When the beam is perpendicular to the crystal, $\hat{n} = \hat{v}$, so equation 31 simplifies to $|\hat{n} \cdot \hat{\Omega}| = |1 - 2\sin^2 \theta_B|$.

Using thi fact to compute f_{geo} allows us to find that $N_0 = 5.15 \times 10^{-7}$ for PXR reflecting from the $(1\bar{1}1)$ in the given geometry. I have assumed the crystal has a thickness of 168 μm .

4.1.3 Rotating the Crystal

Since a detector cannot easily be placed at 109° degrees from the beam axis, it is necessary to rotate the crystal to reflect at 90° with respect to the beam, where the goniometer windows are located. There are two degrees of freedom with which to accomplish this while preserving channeling. First, the crystal can be rotated about the beam axis. This does not change the characteristics of the PXR but only the azimuthal angle of the PXR around the beam. Rotating the crystal 360° degrees about the beam axis, the PXR would sweep out a cone with the tip at the beam-crystal intersection. For the above discussed plane, the cone would point backwards and have a total opening angle of $2 \times (180^\circ - 109.48^\circ) = 141^\circ$.

The other rotational degree of freedom is to rotate the crystal about the normal to the channeling crystal plane, i.e., to rotate about $\frac{1}{\sqrt{2}}(1, 1, 0)$. This rotation does change the Bragg angle and therefore the characteristics of the PXR, and adjusting this angle can adjust the PXR to be reflected at 90° from the beam.

As can be seen from Figure 17, the necessary rotation for the $(1\bar{1}1)$ is particularly simple. The angle of the PXR needs to be changed by $109.48^\circ - 90^\circ = 19.48^\circ$, which implies that the crystal must be rotated in the plane by $19.48^\circ/2 = 9.736^\circ$.

Since not all rotations of every reflecting plane can be predicted geometrically so easily, a matrix transformation representing a more general rotation is given by the Rodrigues rotation matrix, equation 24. For rotations about $\hat{\omega} = \frac{1}{\sqrt{2}}(1, 1, 0)$, this formula reduces to

$$R_{\hat{\omega}}(\psi) = \begin{pmatrix} \cos^2(\psi/2) & \sin^2(\psi/2) & \frac{1}{\sqrt{2}} \sin \psi \\ \sin^2(\psi/2) & \cos^2(\psi/2) & -\frac{1}{\sqrt{2}} \sin \psi \\ -\frac{1}{\sqrt{2}} \sin \psi & \frac{1}{\sqrt{2}} \sin \psi & \cos \psi \end{pmatrix} \quad (32)$$

The rotated vector normal to the surface of the crystal is then

$$\hat{n} = R\hat{v} = \left(\frac{-1}{\sqrt{2}} \cos \psi, \frac{1}{\sqrt{2}} \cos \psi, \sin \psi \right) \quad (33)$$

Similarly, rotating the unit normal to the reflecting $(1\bar{1}1)$ plane, $\frac{1}{\sqrt{3}}(1, -1, 1)$, gives

$$\hat{\tau} = \frac{1}{\sqrt{3}} \left(\cos \psi + \frac{1}{\sqrt{2}} \sin \psi, -\cos \psi - \frac{1}{\sqrt{2}} \sin \psi, \cos \psi - \sqrt{2} \sin \psi \right) \quad (34)$$

Therefore,

$$\hat{n} \cdot \hat{\tau} = \frac{-1}{\sqrt{6}} \left(2 \cos \psi + \sqrt{2} \sin \psi \right) = -\sin \left(\psi + \tan^{-1} \sqrt{2} \right) \quad (35)$$

Setting $|\hat{n} \cdot \hat{\tau}| = \sin \theta_B$ gives

$$\psi = \theta_B - \tan^{-1} \sqrt{2} \quad (36)$$

If we want reflection at 90° , then $\theta_B = \frac{\pi}{4}$, so $\psi = \frac{\pi}{4} - \tan^{-1} \sqrt{2} = -0.1699 \text{ rad} = -9.736^\circ$. This magnitude of rotation agrees with the result from before, and the negative sign indicates that the rotation is clockwise. Additionally, from equation 28, the PXR energy at this angle is $E = 4.257 \text{ keV}$, slightly larger than when the beam was perpendicular to the crystal.

Next, it is necessary to compute N_0 after the rotation, which requires computing again f_{geo} . From equations 9 and 31,

$$f_{geo} = L_a \left(\frac{1}{3} + \frac{2\sqrt{2}}{3} \tan \psi \right) \left[1 - \exp \left(\frac{-3t}{L_a(\cos \psi + 2\sqrt{2} \sin \psi)} \right) \right] \quad (37)$$

which gives $f_{geo} = 16.69 \mu\text{m}$ for 4.257 keV x-rays and $t = 168 \mu\text{m}$. Using this to compute N_0 gives $N_0 = 3.524 \times 10^{-7}$, which is a slight reduction in intensity from the unrotated crystal.

4.2 (202) Plane

The (202) plane is more difficult to visualize geometrically, but the same formalism developed in the last section can be used to understand the PXR properties. Now, rotating $\frac{1}{\sqrt{2}}(1, 0, 1)$ (the unit normal to the (202) plane) through an angle ψ gives

$$\hat{\tau} = \frac{1}{\sqrt{2}} \left(\cos^2(\psi/2) + \frac{1}{\sqrt{2}} \sin \psi, \sin^2(\psi/2) - \frac{1}{\sqrt{2}} \sin \psi, \cos \psi - \frac{1}{\sqrt{2}} \sin \psi \right) \quad (38)$$

so that

$$|\hat{\tau} \cdot \hat{v}| = \frac{\sqrt{3}}{2} \sin \left(\psi + \cot^{-1} \sqrt{2} \right) = \sin \theta_B \quad (39)$$

which for $\theta_B = \frac{\pi}{4}$ implies that $\psi = \cot^{-1}(2\sqrt{2}) = 0.3398 \text{ rad} = 19.47^\circ$. Using equation 28 then implies that $E = 6.952 \text{ keV}$. Note that for $\psi = 0$, $\sin \theta_B = \frac{1}{2} \implies \theta_B = 30^\circ$ so that the PXR would be reflected 60° from the beam axis. This is not an experimentally convenient observation angle.

Unlike the $(1\bar{1}1)$ plane, this reflection, though at 90° to the beam, still does not pass through the windows, which are in the $\pm\hat{z}$ directions. This can be seen by computing $\hat{\Omega}$, the unit vector in the direction of the reflection, at $\psi = \cot^{-1}(2\sqrt{2})$. Using equation 30, $\hat{\Omega} = \frac{1}{2}(1, 1, \sqrt{2})$. To compute what rotation around the beam axis is necessary to rotate $\hat{\Omega}$ into $(0, 0, 1)$, use the Rodrigues rotation matrix for rotations through angle φ about $\hat{v} = \frac{1}{\sqrt{2}}(-1, 1, 0)$,

$$R_{\hat{v}}(\varphi) = \begin{pmatrix} \cos^2(\varphi/2) & -\sin^2(\varphi/2) & \frac{1}{\sqrt{2}}\sin\varphi \\ -\sin^2(\varphi/2) & \cos^2(\varphi/2) & \frac{1}{\sqrt{2}}\sin\varphi \\ -\frac{1}{\sqrt{2}}\sin\varphi & -\frac{1}{\sqrt{2}}\sin\varphi & \cos\varphi \end{pmatrix} \quad (40)$$

Defining $\hat{\Omega}' = R_{\hat{v}}(\varphi)\hat{\Omega}$,

$$\hat{\Omega}' = \frac{1}{2} \left(\cos\varphi + \sin\varphi, \cos\varphi + \sin\varphi, -\sqrt{2}\sin\varphi + \sqrt{2}\cos\varphi \right) \quad (41)$$

From this, it is easy to see that $\hat{\Omega}' = (0, 0, 1)$ when $\varphi = -45^\circ$, which indicates that a 45° rotation around the beam axis is necessary in addition to the 19.47° rotation about the normal to the channeling plane.

Computing f_{geo} gives

$$f_{geo} = \left| \frac{1}{2} - \frac{1}{\sqrt{2}} \tan\psi \right| \left[1 - \exp\left(\frac{-t}{L_a(\cos\psi - \frac{\sqrt{3}}{2}\sin(\psi + \cot^{-1}\sqrt{2}))} \right) \right] \quad (42)$$

which at $\psi = \cot^{-1}(2\sqrt{2})$, $E = 6.952$ keV, and $t = 168$ μm gives $f_{geo} = 87.13$ μm . Therefore, I find $N_0 = 6.529 \times 10^{-7}$. The (202) plane has a larger energy and intensity than the $(1\bar{1}1)$ plane, but at the cost of having a more difficult rotation to have it appropriately aligned.

4.3 $(2\bar{2}0)$ Plane

This plane is directly perpendicular to the beam. This implies that when the crystal is unrotated, the PXR will be reflected directly backwards along the beam. Simply rotating the crystal 45° toward the detector will reflect the PXR in that direction.

When rotated, this plane will reflect PXR with the same energy as the rotated (202) plane, 6.952 keV. However, the geometric factor and therefore the intensity is changed. The new geometric factor at the 45° rotation is

$$f_{geo} = L_a \left(1 - \exp\left(\frac{-t\sqrt{2}}{L_a} \right) \right) \quad (43)$$

which gives $f_{geo} = 182.6$ μm . Therefore, $N_0 = 1.368 \times 10^{-6}$, which is a significant increase in intensity compared to the (202) plane. This suggests that if the setup is free to rotate the crystal, the best plane to use is the $(2\bar{2}0)$ plane, because it has the brightest and highest energy x-rays of all the considered planes. A summary of all these calculations are shown in Table 1. There are other, higher order planes, and though they may have higher energies, they will have N_0 perhaps too low to be of interest.

	E (keV)	N_0	ψ	φ
($1\bar{1}1$)	4.257	3.524×10^{-7}	9.736°	0°
($2\bar{2}0$)	6.952	1.368×10^{-6}	45°	0°
(202)	6.952	6.529×10^{-7}	19.47°	45°

Table 1: Summary of calculations for PXR while channeling, assuming that the PXR will be reflected through a port at 90° to the beam. ψ is a rotation about the normal to the channeling plane, and φ is a rotation about the beam axis. The rotations assume the channeling plane is initially horizontal. Note that PXR while channeling also suffers a $\approx 10\%$ decrease in intensity due to the channeling compared to the same PXR when not channeling [8].

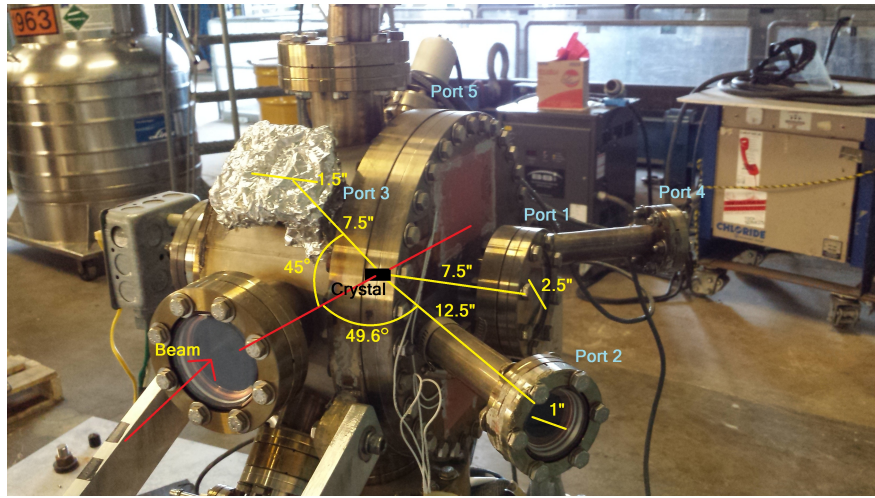


Figure 18: A photograph of the equipment that will be modified to make a new goniometer.

5 Future Goniometer

In the future at ASTA, a new goniometer is going to be constructed using spare photocathode chamber. A photograph of this chamber is shown in Figure 18. This chamber is excellently suited to PXR studies because it has many different ports through which it would be possible to observe PXR at different angles. Additionally, the crystal support could be constructed to be well suited to allow the free escape of PXR, which is a potential problem with the current goniometer. With this goniometer, it could be designed for the PXR experiment without having to simultaneously be convenient for channeling.

Therefore, we could be given free choice in crystal parameters for the PXR, optimizing as much as possible to obtain bright, high energy PXR through any of the available windows. A summary of the calculations for several different planes through several different windows is shown in Table 2.

	(111)		(220)	
	E (keV)	N_0	E (keV)	N_0
Port 1	4.257	1.842×10^{-6}	6.951	7.295×10^{-7}
Port 2	3.316	1.210×10^{-6}	5.415	6.283×10^{-7}
Port 3	3.258	1.172×10^{-6}	5.320	6.200×10^{-7}
Port 4	7.176	3.259×10^{-6}	11.720	8.458×10^{-7}
Port 5	7.866	3.457×10^{-6}	12.845	8.563×10^{-7}
	(311)		(400)	
	E (keV)	N_0	E (keV)	N_0
Port 1	8.152	1.972×10^{-7}	9.831	1.889×10^{-7}
Port 2	6.350	1.800×10^{-7}	7.658	1.797×10^{-7}
Port 3	6.239	1.785×10^{-7}	7.524	1.788×10^{-7}
Port 4	13.742	2.152×10^{-7}	16.575	1.973×10^{-7}
Port 5	15.062	2.167×10^{-7}	18.166	1.978×10^{-7}

Table 2: Properties calculated if the crystal is cut in the Bragg geometry (reflecting planes parallel to incident surface), which is the optimal cut. The crystal thickness $168 \mu\text{m}$ so that the N_0 can be directly compared to those of PXR while channeling.

Based on the table, optimal intensity would be obtained with PXR reflected from the (111) plane out Port 5 (see Figure 18). Optimal energy, however, can be obtained with the (400) plane at 18 keV, but it suffers an order of magnitude reduction in intensity.

References

- [1] Neil W Ashcroft and N. David Mermin. *Solid State Physics*. Cengage Learning, 1976.
- [2] Serge Belongie and MathWorld-A Wolfram Web Resource. Rodrigues' rotation formula.
- [3] K. H. Brenzinger et al. How narrow is the linewidth of parametric x-ray radiation. *Phys. Rev. Lett.*, 1997.
- [4] C.T. Chantler et al. X-ray form factor, attenuation, and scattering tables, 2005.
- [5] J. Beringer et al. Review of Particle Physics. *Phys. Rev. D*, 86:010001, (2012) and 2013 Partial Update for the 2014 Edition.
- [6] J. Freudenberger et al. Lineshape, linewidth and spectral density of parametric x-radiation at low electron energy in diamond. *Appl. Phys. Lett.*, 70:267, 1997.
- [7] Charles Kittel. *Introduction to Solid State Physics*. Wiley, 2004.
- [8] K. B. Korotchenko, Yu. L. Pivovarov, and Y. Takabayashi. Experimental and theoretical study of pxrc (parametrix x-radiation at channeling) from 255 mev electrons in si. 2013.
- [9] John Quintana. f0 intertables, 2002.
- [10] B. Sones, Y. Danon, and R. C. Block. X-ray imaging with parametric X-rays (PXR) from a lithium fluoride (LiF) crystal. *Nucl. Inst. and Meth. A*, 560:589–597, 2006.
- [11] Bryndol Sones, Y. Danon, and R. C. Block. *Development of a Novel Tunable X-Ray Source for the RPI-Linac*. PhD thesis.

Acknowledgements

I would like to first thank my mentor Tanaji Sen for guiding me through this project. I would also like to thank Eric Prebys for being an excellent head of the Lee Teng program and Tanja Waltrip for organizing the intern programs so well.

A Plots of Various Crystal Parameters

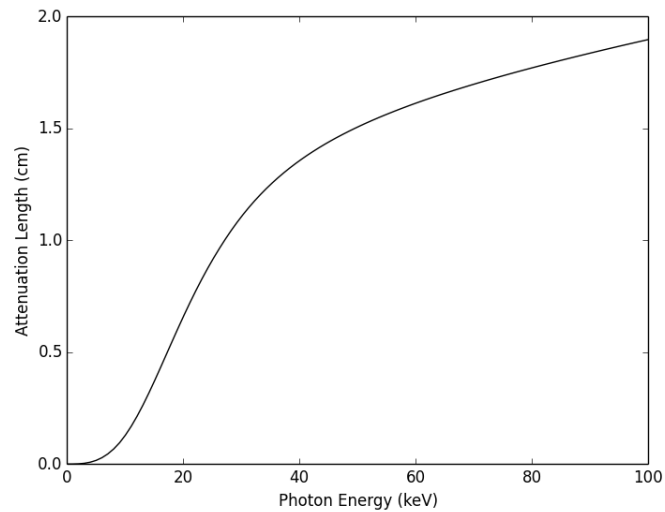


Figure 19: A plot of how the attenuation length of x-rays in diamond depends on the x-ray energy.

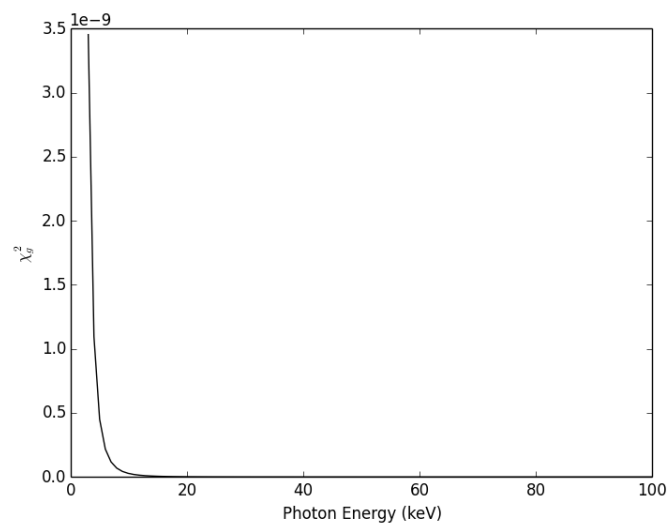


Figure 20: A plot of how the magnitude of the Fourier transform of the electric susceptibility (χ_g^2) depends on the x-ray energy. Notice the sharp drop then tends to disfavor the production of PXR at higher energies.

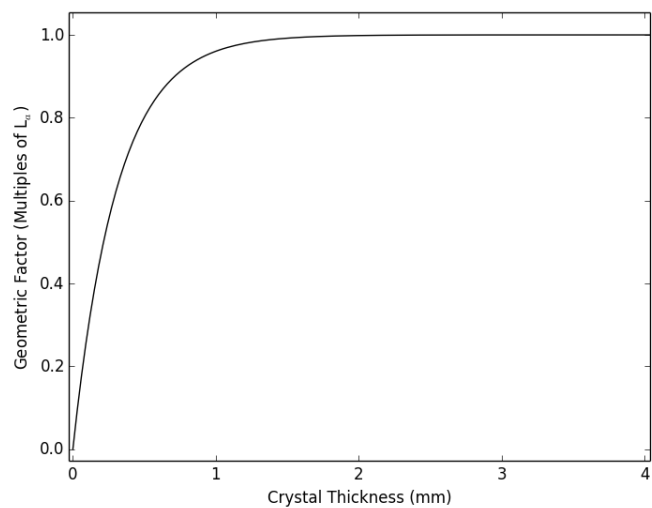


Figure 21: The dependence of the geometric factor on the thickness of the crystal.

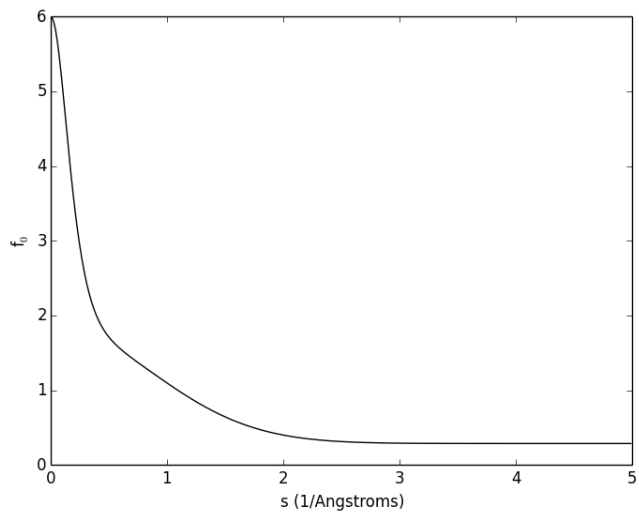


Figure 22: The f_0 parameter which is used in equation 11 and defined in equation 12.

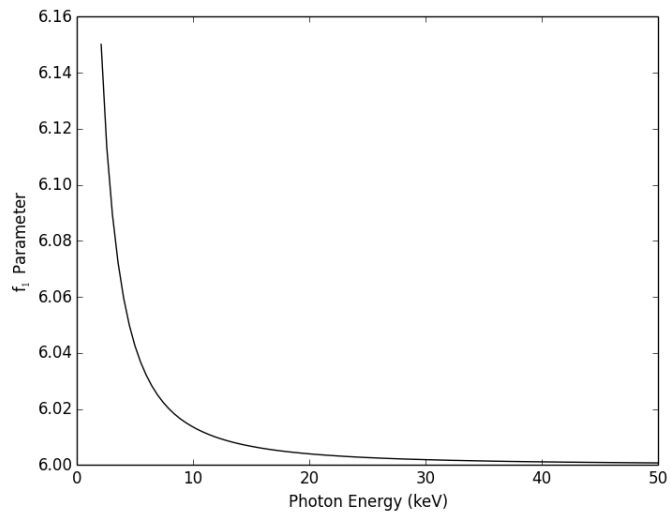


Figure 23: The f_1 parameter which is used in equation 11.

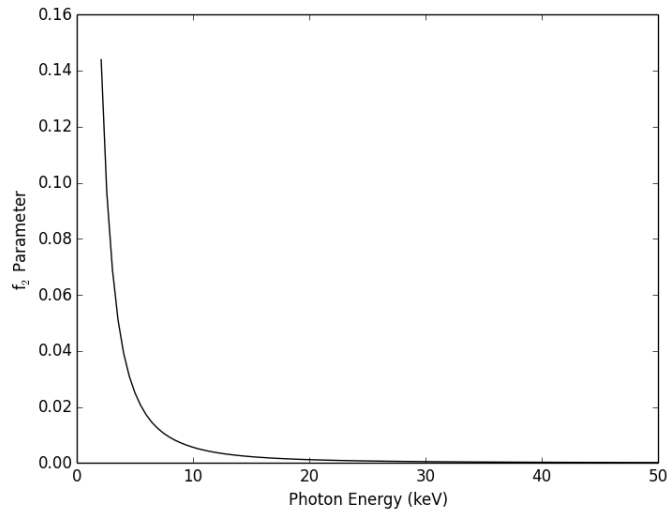


Figure 24: The f_2 parameter which is used in equation 11.